PCCP

Accepted Manuscript

ROYAL SOCIETY OF CHEMISTRY

www.rsc.org/pccp

Journal Name

ARTICLE

Photoluminescence of cerium fluoride and cerium-doped lanthanum fluoride nanoparticles and investigation of energy transfer to photosensitizer molecules

Daniel R. Cooper,[a] Konstantin Kudinov,[c] Pooja Tyagi,[b] Colin K. Hill,[d] Stephen E. Bradforth[c] and Jay L. Nadeau[a]

$Ce_xLa_{1-x}F_3$ nanoparticles have been proposed for use in nanoscintillator-photosensitizer systems, where excitation of nanoparticles by ionizing radiation would result in energy transfer to photosensitizer molecules, effectively combining the effects of radiotherapy and photodynamic therapy. Thus far, there have been few experimental investigations of such systems. This study reports novel synthesis methods for water-dispersible $Ce_{0.1}La_{0.9}F_3/LaF_3$ and CeF_3/LaF_3 core/shell nanoparticles and an investigation of energy transfer to photosensitizers. Unbound deuteroporphyrin IX 2,4-disulfonic acid was found to substantially quench the luminescence of large (>10 nm diameter) aminocaproic acid-stabilized nanoparticles at reasonable concentrations and loading amounts: up to 80% quenching at 6% w/w photosensitizer loading. Energy transfer was found to occur primarily through a cascade, with excitation of "regular" site Ce^{3+} at 252 nm relayed to photosensitizer molecules at the nanoparticle surface through intermediate "perturbed" Ce^{3+} sites. Smaller (<5 nm) citrate-stabilized nanoparticles were coated with the bisphosphonate alendronate, allowing covalent conjugation to chlorin e6 and resulting in static quenching of the nanoparticle luminescence: ~50% at ~0.44% w/w. These results provide insight into energy transfer mechanisms that may prove valuable for optimizing similar systems.

Introduction

Inorganic nanoparticles (NPs) doped with lanthanides have emerged as a versatile collection of materials for a range of potential optical and medical applications. Robust luminescence, low toxicity, and chemical stability make them an appealing choice for bioprobes and theranostics. The use of NPs as a means of drug delivery is an extremely active field of research, and in addition to a range of chemotherapeutic agents, photosensitizer (PS) molecules have become a popular choice for coupling to luminescent NPs[1-8]. Photodynamic therapy (PDT) takes advantage of selective activation of PS molecules, which have minimal innate toxicity but which can produce reactive oxygen species (ROS) upon absorption of light. Considerable efforts have gone toward the development of

upconverting NPs (UCNPs) that circumvent issues of tissue transparency by producing tunable visible/infrared emission upon near-infrared excitation, allowing for deeper imaging[9-11] and/or indirect PS activation[12-16] in the "water window." A relatively unexplored approach to deep-tissue activation is to use radioluminescent or scintillating NPs that emit tunable UV/visible light upon excitation by highly penetrating ionizing radiation. As radiotherapy is used widely in clinical settings, a nanoscintillator-photosensitizer system may provide a means to radiosensitize malignant tissues through high-Z enhancement[17-19] combined with therapeutic effects of photosensitizers[20-26].

$Ce_xLa_{1-x}F_3$ is a heavy scintillator that has been investigated as bulk single crystals[27-32] and more recently at the nanoscale[33, 34]. LaF_3 is a good host for the luminescence of Ce^{3+} dopants due to its optical transparency, large band gap, and low phonon

energy. Due to the chemical similarly between trivalent lanthanum and cerium, one can be fully substituted for the other without significantly affecting the physical properties of the crystal. Ce^{3+} is distinct from other luminescent lanthanides because of parity-allowed $5d$–$4f$ transitions that are notably sensitive to the environment due to a lack of shielding by outer electrons. The luminescence of $Ce_xLa_{1-x}F_3$ spans the UVA & UVB into the UVC & blue, with the shape of the emission profile and luminescence yield depending on the dopant concentration and crystal quality. While the emission wavelengths are appropriate for exciting photosensitizers, most of which have strong absorbance bands in the UVA/blue, the mechanisms of nanoscintillator luminescence and energy transfer (ET) have yet to be thoroughly assessed. In particular, surface effects are of critical importance at the nanoscale, so particles of different sizes might display very different behavior[35, 36].

Two compositions of NPs were chosen for this study: $Ce_{0.1}La_{0.9}F_3$ and CeF_3. Despite the substantial difference in cerium content, the scintillation yields of bulk single crystals were found to be comparable: beyond 10% Ce^{3+} doping, increased radiation trapping resulted in only a modest increase in radioluminescence. Nanoparticles of both compositions were synthesized using hydrothermal techniques and modified by the addition of undoped LaF_3 shells to improve luminescence yields through surface site passivation, though it has been established that cation exchange during aqueous synthesis may lead to more complex gradient structures rather than well-defined core/shell structures[37, 38]. Water-dispersible, platelet-like NPs were synthesized with aminocaproic acid ligands and mixed with the photosensitizer deuteroporphyrin IX 2,4-disulfonic acid (DPIX-DS) to investigate mechanisms of energy transfer in electrostatic complexes.

A separate synthesis technique using citric acid ligands was employed to produce smaller, more spherical NPs, which were functionalized for bioconjugation through ligand exchange with alendronic acid, a bisphosphonate drug. Alendronate provides a strong association to the NP surface through bisphosphonate groups, as well as free amine functional groups for bioconjugation. The photosensitizer chlorin e6 (Ce6) was conjugated to the alendronate-coated NPs through amide bond formation to investigate energy transfer with covalently bound PS molecules.

As a prelude to experiments using excitation by ionizing radiation, here we have investigated the NPs and photosensitizer complexes and conjugates through steady-state and time-resolved photoluminescence (PL) spectroscopy, in order to provide insight that may be valuable toward maximizing energy transfer between luminescent Ce^{3+}-doped NPs and photosensitizers. We have determined that energy transfer to photosensitizers occurs efficiently through excitation of the NPs, with distinct populations of Ce^{3+} acting as energy relays.

Experimental section

Materials

Lanthanum(III) chloride heptahydrate (99.999%), cerium(III) chloride heptahydrate (99.999%), lanthanum(III) nitrate hexahydrate (99.999%), cerium(III) nitrate hexahydrate (99%, 1-2% La), 6-aminocaproic acid (≥99%) and citric acid (ACS, ≥99.5%) were purchased from Sigma-Aldrich and used without modification. Ammonium hydroxide (ACS) was purchased from ACP Chemicals Inc. Photosensitizers deuteroporphyrin IX 2,4-disulfonic acid dihydrochloride and chlorin e6 were purchased from Frontier Scientific. N-hydroxysuccinimide (>98%) and alendronate sodium trihydrate (97%) were purchased from Alfa Aesar.

Synthesis of aminocaproic acid-stabilized $Ce_xLa_{1-x}F_3/LaF_3$ (x = 0.1 or 1) "core/shell" nanoparticles

Water-dispersible aminocaproic acid-stabilized NPs (ACA-NPs) were synthesized using a one-pot hydrothermal technique. NP cores were prepared by first dissolving 30 mmol (3.94 g) of aminocaproic acid (ACA) and 0.5 mmol of lanthanide chloride hydrates in 35 mL of water in a 250 mL three-neck flask: $Ce_{0.1}La_{0.9}F_3$ core precursor solution consisted of 0.45 mmol (167 mg) $LaCl_3 \cdot 7H_2O$ and 0.05 mmol (18.6 mg) $CeCl_3 \cdot 7H_2O$; CeF_3 core precursor solution consisted of 0.5 mmol (186.3 mg) $CeCl_3 \cdot 7H_2O$. Fluoride precursor solution was prepared by dissolving 1.5 mmol (63 mg) NaF in 2 mL water and purging with N_2 gas for several minutes. The lanthanide solution was stirred and purged with N_2 gas for an hour at room temperature and then heated to 75 °C, at which point the fluoride precursor solution was rapidly injected. The solution was stirred at 75 °C for 2 hours before addition of the shell.

For the addition of undoped LaF_3 shells, lanthanum and fluoride solutions were prepared and alternately added dropwise in 10 fractions each over ~20 minutes. Lanthanum solutions contained 0.5 mmol (186 mg) $LaCl_3 \cdot 7H_2O$ in 2 mL water, and fluoride solutions 1.5 mmol (63 mg) NaF in 2 mL water. After addition, the core/shell NP solution was stirred at 75 °C for 2 hours, then allowed to cool to room temperature.

To remove excess reagents, the NPs were precipitated by the addition of ~360 mL of ethanol followed by centrifugation at 8,000 × g for 8 minutes. The NPs were collected as a translucent pellet, resuspended in ~10 mL of water, then filtered through a two-stage Millex 0.45/1.0 μm PVDF/APFB syringe filter. Stock solutions containing ~20-30 mg/mL of NPs appeared transparent.

Non-covalent association of deuteroporphyrin IX 2,4-disulfonic acid with ACA-NPs

Deuteroporphyrin IX 2,4-disulfonic acid dihydrochloride (DPIX-DS) was dissolved at 1 mg/mL in water and diluted into aqueous NP solutions at 1-12% w/w of the NPs to be investigated. No pH correction was done. NP-PS samples were diluted ten-fold for steady-state PL and TCSPC measurements to avoid inner-filter effects.

Synthesis of citrate-stabilized $Ce_{0.1}La_{0.9}F_3/LaF_3$ "core/shell" nanoparticles

Water-dispersible citrate-stabilized NPs (CA-NPs) were synthesized using a slightly modified hydrothermal method developed elsewhere[39, 40]. First, 10.4 mmol (2 g) of citric acid was dissolved in 35 mL water and partially neutralized with 28% NH_4OH to pH 5-6, then the solution was heated to 75 °C with stirring. Lanthanide precursor solutions were prepared by dissolving 1.33 mmol lanthanide nitrate hydrates in 2 mL methanol: $Ce_{0.1}La_{0.9}F_3$ core precursor solution consisted of 1.197 mmol (518.3 mg) $La(NO_3)_3 \cdot 6H_2O$ and 0.133 mmol (57.8 mg) $Ce(NO_3)_3 \cdot 6H_2O$. Fluoride precursor solution was prepared by dissolving 8.38 mmol (352 mg) NaF in 10 mL water. The lanthanide solution was then added to the heated citric acid solution dropwise, followed by the addition of the fluoride solution dropwise. The solution was stirred at 75 °C for 2 hours before addition of the shell.

For the addition of undoped LaF_3 shells, a solution of 1.33 mmol (576 mg) $La(NO_3)_3 \cdot 6H_2O$ was prepared and added dropwise. The NP solution was stirred at 75 °C for an additional 2 hours, then allowed to cool to room temperature.

To remove excess reagents, the NPs were precipitated by the addition of ~50 mL of ethanol followed by centrifugation at 4,000 RPM for 3 minutes. The white NP pellets were washed with 95% ethanol followed by centrifugation at 4,000 RPM for 3 minutes. The previous step was repeated, then the NP pellet was resuspended in ~25 mL of water and filtered through a two-stage Millex 0.45/1.0 μm PVDF/APFB syringe filter. Stock solutions containing ~20-30 mg/mL of NPs appeared transparent.

Ligand exchange of CA-NPs with alendronate and conjugation to chlorin e6

Citrate-stabilized NPs were coated with alendronate by ligand exchange in water. 100 mg of alendronate sodium trihydrate was dissolved in 30 mL water and 100 mg NPs (~4 mL) were added under stirring. The solution was heated at 60 °C and stirred for 2 hours, becoming turbid after several minutes. NPs were pelleted by centrifugation at 12,000 × g for 15 minutes and the supernatant discarded. The pale blue glassy NP pellet was first redissolved in ~4 mL 0.1 M HCl then precipitated by the addition of ~40 mL ethanol and centrifugation at 12,000 × g for 15 minutes. The previous step was repeated, and the pellet of alendronate-stabilized NPs (ALE-NPs) was then dissolved in ~4 mL water.

Chlorin e6 (Ce6) conjugates were prepared by first dissolving 2 mg Ce6 in 4 mL DMSO, followed by the addition of 1 mL of 50 mM (~5.8 mg) N-hydroxysuccinimide (NHS) in DMSO and 6.2 μL of *N,N'*-diisopropylcarbodiimide (DIC), then were stirred for 30 minutes. 1 mL (~20 mg) of ALE-NPs was added quickly under heavy stirring. The reaction vial was protected from light and stirred for 18-20 hours. Conjugates were isolated from excess reagents and DMSO by addition of ~40 mL ethanol and NaCl to 10 mM (typically 90 μL of 5 M NaCl in water), followed by centrifugation at 12,000 × g for 15 minutes. The glassy green pellet was redissolved in ~2 mL of 0.1 M HCl and precipitated by the addition of ~30 mL ethanol and centrifugation at 12,000 × g for 15 minutes. The previous

step was repeated, then the NP-PS pellet was dissolved in ~1 mL water.

Characterization of NPs

NP size, morphology and crystallinity were evaluated from high resolution transmission electron microscopy (HR-TEM) and selected area electron diffraction (SAED) images acquired with a Philips CM200 TEM operating at 200 kV. Samples were prepared by drop casting 5 μL of a diluted NP solution onto a grid and air-drying overnight.

The mass concentrations of the NPs were determined by drying several mL of the as-synthesized NP stock solutions under vacuum with a rotary evaporator. Mass extinction coefficients were then determined by measuring the absorbance of successive dilutions of the NPs in water and fitting the A_{250} values to a line. The values include the ligand mass contributions.

Time-resolved and steady-state photoluminescence

Photoluminescence decays were obtained by the time-correlated single photon counting (TCSPC) technique. 800 nm laser pulses (~70 fs) out of a Coherent RegA 9050 Ti/sapphire regenerative amplifier operating at 250 kHz repetition rate were coupled into an OPA (Coherent 9450) which produced 504 nm light with an average power of ~30 mW. The OPA output was directed through a fused silica prism pair for pulse compression prior to a type I BBO doubling crystal. The resulting 252 nm output passed through a calcium-fluoride prism pair compressor primarily to spectrally clean the 252 nm pulses. The 252 nm beam was gently focused into the sample with a large focal spot diameter of 0.785 mm. The excitation power was ~2.4 mW, with peak pulse intensities at the sample of 1×10^7 W/cm^2 with $5\text{-}50 \times 10^{-6}$ J/cm^2 fluence after attenuation of the 252 nm excitation beam with neutral density filters placed before the focusing lens. The luminescence was collected with a 3.5 cm focal length lens placed perpendicular to the excitation beam and the collimated luminescence focused into a monochromator with a 10 cm focal length lens. The monochromator was a CVI CMSP112 double spectrograph with a 1/8 m total path length in negative dispersive mode with a pair of 600 groove/mm gratings (overall f number 3.9). The slit widths were 1.2 mm and based on a monochromator dispersion of 14 nm/mm, provided 10 nm resolution. A Hamamatsu RU3809 microchannel-plate photomultiplier was mounted on the monochromator exit slit. A Becker and Hickl SPC-630 photon counting board was used to record the time-resolved emission. The reference signal was provided by a portion of the excitation beam sent to a fast photodiode. To ensure good statistics, count rates were held at <1% of the laser repetition rate to avoid pulse pile up. Typical acquisition times were 10 minutes for a single scan. Lifetime decays of NPs were measured at 285 nm, 300 nm, 330 nm and 380 nm.

The instrument response function (IRF) was determined from scatter off a solution of dilute coffee creamer. The full width at half-maximum of the IRF was 37 ps. IRF reconvolution, multiexponential decay fits and intensity-

weighted average lifetime calculations were performed using FluoFit 4.0 (PicoQuant, Berlin). Goodness-of-fit data and residuals were used to gauge fit results; a χ^2 between 0.9-1.1 and random distribution of residuals around the x-axis were necessary for a fit to be considered accurate. Lifetime decay contributions were weighted by fractional intensity. Negative amplitude decays (representing the rise times) were included in the calculation of average lifetime values, but not for fractional decay intensities. Multi-exponential decay fits were of the form

$$I(t) = \int_{-\infty}^{t} IRF(t') \sum_{i=1}^{n} A_i e^{-\frac{t-t'}{\tau_i}} \, dt'$$

where IRF(t') is the instrument response function. UV−visible absorbance spectra were taken with a Varian Cary 50 spectrometer or Molecular Devices SpectraMax Plus 384. Steady-state emission spectra were recorded with either a Horiba FluoroLog-3 spectrofluorometer (5 nm excitation and emission slit widths and corrected for variations in lamp intensity, Figures 2 & 3), a Varian Cary Eclipse spectrophotometer (5 nm excitation and emission slit widths, Figures 7 & 10), or Molecular Devices SpectraMax i3 (QY measurements). Emission spectra in Figures 3c & d are shown in arbitrary units proportional to the original data in counts per second. All spectra were recorded in quartz cuvettes and were averaged from ten consecutive scans, with the exception of absorbance spectra in Figures 8 & 10, which were recorded in UV-transparent plastic "UVettes." Fitting of steady-state PL spectra using Gaussian functions was done using the Matlab Curve Fitting Toolbox with no constraints on the parameters.

Relative NP PL quantum yields (Φ_{NP}) were determined using standard methods by comparison to L-tryptophan in water ($\Phi_s = 0.12$)[41] using the equation

$$\phi_{NP} = \phi_s \left(\frac{F_{NP}}{A_{NP}}\right)\left(\frac{A_s}{F_s}\right)\left(\frac{n_{NP}}{n_s}\right)^2$$

where F is the integrated intensity (using 250 nm excitation), A is the absorbance at 250 nm, and n is index of refraction of the solvent. For each sample, the emission intensity was measured for six dilutions and fit to a line of A_{250} vs. integrated emission, giving the F/A values which were used to calculate the QY (Figure S1). The fits were not forced through the origin as the background fluorescence of the multi-well plates could not be entirely accounted for. All measurements were taken at room temperature.

Results

Characterization and photoluminescence of ACA-stabilized NPs and DPIX-DS complexes

TEM images of ACA-NPs revealed roughly hexagonal platelet morphology, as shown in Figure 1. For measurements and calculations, they were approximated as thin cylinders.

$Ce_{0.1}La_{0.9}F_3/LaF_3$ NPs had an average diameter of 11.9 ± 3.5 nm (n = 208) and an average thickness of 3.2 ± 0.5 nm (n = 33). CeF_3/LaF_3 NPs were noticeably larger, with an average diameter of 16.4 ± 3.9 nm (n = 218) and an average thickness of 4.3 ± 0.7 nm (n = 40) – giving ~1.9 times the surface area and ~2.6 times the volume and molar mass compared to the $Ce_{0.1}La_{0.9}F_3/LaF_3$ NPs (details shown in Table S1).

Consistent with prior work in bulk and nanocrystals, primarily that of Wojtowicz *et al*. and Jacobsohn *et al*., the steady-state PL spectra of both NP compositions could be fit well by a sum of Gaussian functions (Figure 2a & b, Table 1). The three major components arise from the transitions from the lowest excited Ce^{3+} *5d* level to the spin-orbit split *4f* ground states $^2F_{5/2}$ (G_1) and $^2F_{7/2}$ (G_2), as well as a broad, lower energy band arising from Ce^{3+} residing in perturbed sites (G_3). Importantly, the reduced *5d*–*4f* energy gap of Ce^{3+} in perturbed sites enables radiation trapping from regular sites by nonradiative transfer or re-absorption of emission. These "bulk-type" perturbations are believed to arise from crystallographic defects involving fluorine vacancies, likely Frenkel disorder. As each cation has 11 nearest F⁻ neighbors at distances from 2.421 Å to 2.999 Å, the degree of perturbation varies and results in an inhomogeneous broadening of energy levels. Ce^{3+} sites at or near the surface of the NPs that are incompletely passivated by the shell are further affected by asymmetry and local distortions in the crystal lattice[34], leading to additional bathochromic shift of the emission as well as luminescence quenching by high energy vibrations of water and organic ligands. The fourth low-amplitude, low-energy component, G_4, is believed to be associated with the surface sites. As-synthesized NPs were found to have fairly similar QY values: 0.17 for $Ce_{0.1}La_{0.9}F_3/LaF_3$ and 0.21 for CeF_3/LaF_3.

Excitation at 252 nm is primarily absorbed by regular site Ce^{3+} ions followed by energy transfer from regular site donors to perturbed site acceptors at a rate $W = \alpha/r^6$, where α is a transfer rate constant and r is the distance between any two such sites. For nearest neighbors in bulk crystals ($r = 4.1$ Å), the rate has been calculated to be 1.56×10^9 s⁻¹, roughly 1-1.5 orders of magnitude faster than the radiative rate[31]. Between sites of the same type (regular-regular and perturbed-perturbed), the transfer rates are expected to be significantly slower than the radiative rates, on the order of 10^5 s⁻¹. Even at 10% Ce^{3+} doping in NPs (where r is greater, provided uniform distribution of dopants), the efficiency of this transfer resulted in more than half of the steady-state emission arising from perturbed sites (A_3/A_{tot} in Table 1), increasing to ~88% for CeF_3/LaF_3 NPs. Indeed, the prominence of perturbed site emission has been reported in LaF_3 NPs (synthesized with ammonium di-*n*-octadecyldithiophosphate ligands in water) at Ce^{3+} doping as low as 1.3%[34].

To investigate NP-PS interactions, water-soluble DPIX-DS was added to NPs in water at 1-12% w/w and mixed briefly. DPIX-DS was chosen for its water-solubility (due to degree and symmetry of negative charge from carboxylic acid and sulfonic acid groups, also encouraging association with the positively-charged NPs). Like many PS molecules, DPIX-DS tends to

aggregate, forming non-fluorescent dimers above certain concentrations in aqueous solution[42], which we have corroborated by observing a change in absorbance character of free DPIX-DS in solution at ~5 μg/mL (Figure S2). All PL measurements were taken with DPIX-DS at <5 μg/mL, in the monomeric regime. Absorbance measurements of the ACA-NPs alone and with added DPIX-DS are shown in Figure 3a & b. Note the absorption of the NPs shown here (primarily at λ <260 nm) is due to Ce^{3+}, and so CeF_3/LaF_3 NPs of a given size absorb ~10X as strongly as $Ce_{0.1}La_{0.9}F_3/LaF_3$ NPs of the same size.

Addition of DPIX-DS to the NPs quenched the steady-state PL of the NPs in a concentration-dependent fashion. The spectra are shown in Figure 3c & d. The distinct peaks of the emission components can be easily resolved by eye starting at 6% w/w DPIX-DS for both NP types, and a bathochromic shift is apparent in the CeF_3/LaF_3 peak (roughly corresponding to the perturbed band peak), from 336 nm in the absence of DPIX-DS to 352 nm at 12% w/w DPIX-DS. The quenching efficiency $\eta = 1 - I/I_0$ is shown in Figure 4, where I and I_0 are the integrated intensities in the presence and absence of PS respectively. The quenching showed a similar trend with both types of NP and exceeded 80% for both types at 6% w/w DPIX-DS. It is not immediately apparent that this should be the case, considering the different sizes and Ce^{3+} concentrations of the NP types, and the NP concentration difference between the samples. For a given % w/w of DPIX-DS, there were ~40% more DPIX-DS molecules per square nanometer of NP surface for CeF_3/LaF_3 NPs (for instance, 2% w/w was equivalent to ~0.10 molecules/nm² with $Ce_{0.1}La_{0.9}F_3/LaF_3$ and ~0.14 molecules/nm² with CeF_3/LaF_3). Details are shown in Table S2. Compared to radioexcitation, where a high degree of cerium concentration-dependent self-quenching is expected, photoexcitation of NPs alone did not result in Ce^{3+} concentration-dependent luminescence quenching (as evidenced by the PL QY values of the NPs), and so the CeF_3/LaF_3 NPs effectively presented many more Ce^{3+} donors per NP (and per surface area) than the $Ce_{0.1}La_{0.9}F_3/LaF_3$ NPs. This became particularly apparent through Stern-Volmer fits of I_0/I values as a function of the absolute DPIX-DS concentrations (shown in Figure S3) which gave markedly different results for each NP type: quenching of $Ce_{0.1}La_{0.9}F_3/LaF_3$ NPs with 1-5% w/w DPIX-DS was best fit by a linear equation of the form

$$\frac{I_0}{I} = 1 + K_{SV}[PS]$$

where [PS] is the molar concentration of DPIX-DS, giving the dynamic quenching constant $K_{SV} = 0.52 \times 10^6 \text{ M}^{-1}$. Quenching of CeF_3/LaF_3 NPs, with DPIX-DS at 2-12% w/w, was best fit by a modification of the model incorporating an additional quenching factor to account for the non-linear behavior, of the form

$$\frac{I_0}{I} = (1 + K_{SV}[PS])e^{(K_q[PS])}$$

where K_q is a constant proportional to the volume of the static "quenching sphere" of the NPs[43]. The fit gave $K_{SV} = 3.38 \times 10^6$ M^{-1} and $K_q = 0.31 \times 10^6 \text{ M}^{-1}$. The K_q parameter is the product of N_A and the quenching volume V_q, leading to $V_q = \sim 0.5$ attoliters, or a sphere of ~50 nm radius. It is apparent from the fit values that the CeF_3/LaF_3 NPs were more efficiently quenched by DPIX-DS, which is unsurprising given the difference in Ce^{3+} content. It is important to note that the pronounced difference in quenching between NP types is not expected to extend to the case of radioexcitation, where each of the NP compositions is expected to be similar in terms of excitation and scintillation output for a given NP size.

The steady-state fits and NP-PS absorbance data were evaluated to determine informative wavelengths for time-resolved measurements: 285 nm (near the peak of the $^2D_{3/2} \rightarrow ^2F_{5/2}$ emission), 300 nm (near the peak of the $^2D_{3/2} \rightarrow ^2F_{7/2}$ emission), 330 nm (near the peak of the perturbed site band), and 380 nm (near the peak of the PS absorbance). With the exception of some 285 nm lifetime decays, each measurement could be fit to a sum of up to four exponential decay functions, depending on the detection wavelength and amount of added PS. Fits were chosen to give a self-consistent description of the system. 300 & 330 nm were taken to be the most representative measurements and will be the focus of the analysis.

PL lifetime decays of NPs alone were found to be consistent with the physical model of direct excitation of regular sites followed by radiation trapping by perturbed sites: fits of measurements made at 300 nm contained major components suggesting regular and perturbed site emission, whereas those made at 330 & 380 nm (entirely within the perturbed site band) contained longer-lived components with rising edges (shown in Figure 2c). Assignment of the components was fairly intuitive for $Ce_{0.1}La_{0.9}F_3/LaF_3$ NPs: 300 nm data was dominated by two decays, 8.13 ns (20%) ascribed to regular sites & 26.8 ns (79%) from perturbed sites; 330 & 380 nm were each fit by mono-exponential decays of 32.5 ns & 38.8 ns respectively. Interpretation of the CeF_3/LaF_3 decays (shown in Figure 2d) was less straightforward. At 300 nm, an adequate fit required four exponentials: 0.34 ns (9.4%), 1.83 ns (27%), 6.36 ns (35%), and 19.1 ns (29%). The steady-state fits suggest this measurement contains primarily perturbed site emission with some regular site contribution. The four exponential fit is likely a semi-arbitrary discretization of Ce^{3+} populations based on the degree of surface quenching, similar to what has been seen in Ce^{3+}–doped YAG[44], as well as $LaPO_4$ and LaF_3 NPs doped with a variety of trivalent lanthanides[45]. Two exponentials were required to fit 330 & 380 nm data, likely a simpler distinction between the "interior" perturbed population (with lifetimes close to those found with $Ce_{0.1}La_{0.9}F_3/LaF_3$ NPs) and the "surface" perturbed population (with shorter lifetimes). In addition to the prominent decays, both types of NPs displayed one or two weak, fast components (mostly <2 ns) that become

increasingly apparent at all measured wavelengths coincident with the quenching of the other components by the addition of DPIX-DS. Full TCSPC fit results are provided in Table S3. The average PL lifetimes of ACA-NPs alone measured at different Ce^{3+} emission wavelengths are shown in Table 2.

Addition of DPIX-DS resulted in quenching of PL lifetimes measured at 300 & 330 nm, likely reflecting energy transfer from the perturbed sites to DPIX-DS (more favorable than from regular sites due to greater spectral overlap and association with the NP surface), and resultant quenching of the regular sites by repopulation of the quenched perturbed sites. This is shown for 0, 2, 4 & 6% w/w DPIX-DS in Figure 5a & b and Table S3. The rising edge associated with the build-up of perturbed site excited states is no longer discernable at ≥3% w/w DPIX-DS, and the 330 nm lifetime decays begin to resemble those at 300 nm (shown in Figure 5c & d). These changes are consistent with an energy transfer cascade of the form regular Ce^{3+}→perturbed Ce^{3+}→PS, as illustrated in Scheme 1. Fits of perturbed site PL decays required additional exponentials with increasing PS concentrations. For $Ce_{0.1}La_{0.9}F_3/LaF_3$ NPs, splitting of the mono-exponential decay of the bare NPs reflects a distinction between sites close enough to the surface to act as the most effective donors, and those in the NP interior. For CeF_3/LaF_3 NPs, the longest lifetime component at 300 nm disappears as the perturbed site band recedes.

Interestingly, average lifetimes measured at 380 nm increased gradually with addition of DPIX-DS. Lifetimes of CeF_3/LaF_3 at 330 nm also increased above 6% w/w. We noted that the 380 nm fits consisted of one component that was quenched as expected, and another that increased to 42.7 ns (for $Ce_{0.1}La_{0.9}F_3/LaF_3$) and 44.5 ns (for CeF_3/LaF_3), lifetimes similar to those found in some bulk CeF_3 crystals. Based on an observed loss of colloidal stability at high PS loading, this may be due to aggregation of NPs, leading to increased reabsorption of higher-energy emission and increasing the apparent lifetime of the low-energy population. This is consistent with the bathochromic shift of the CeF_3/LaF_3 emission. Internal conversion rates from S_n→S_1 in excited DPIX-DS are likely sufficiently fast to preclude PS→perturbed site back-transfer.

Characterization and photoluminescence of CA- and ALE-NPs and chlorin e6 conjugates

TEM images of CA- and ALE-NPs are shown in Figure 6. The images are consistent with previous studies that confirm that the particles are roughly spherical with a diameter of ~4 nm[39]. SAED confirms the small size of the NPs and the preservation of crystallinity after the ligand exchange process.

The general approach to alendronate ligand exchange and chlorin e6 (Ce6) conjugation is shown in Scheme 2, with full details found in the Experimental Section. After isolation of alendronate-exchanged NPs, the citrate absorbance peak around 210 nm disappeared (Figure S4). The presence of alendronate on the NPs was corroborated by EDX spectra showing the phosphorus K_α line around 2 keV (Figure S5). Colloidal stability of the ALE-NPs was found to be sensitive to small

changes in the ionic strength and pH of the solution, with precipitation resulting from an increase of either.

As-synthesized citrate-stabilized $Ce_{0.1}La_{0.9}F_3/LaF_3$ NPs were found to have a QY of 0.06. Steady-state PL spectra could be fit to a sum of four Gaussian functions as with ACA-NPs, though with significant differences in their positions and amplitudes, as shown in Figure 7a. In particular, the $^2D_{3/2}$→$^2F_{7/2}$ (G_2) component was found to be considerably weaker, whereas the contribution of the G_4 component increased, likely due to the larger proportion of surface sites in the smaller NPs. As the surface sites are shifted to lower energies, it is likely that the G_2 component is quenched relative to G_1 because of increased energy transfer to the surface sites. PL lifetime fits (Figure 7c) required additional exponentials compared to ACA-NPs and average lifetimes were somewhat shorter: 16.9 ns at 300 nm, 28.4 ns at 330 nm and 37.6 ns at 380 nm. These effects can also be attributed to the increased prominence of the surface sites and surface quenching. Ligand exchange with alendronate caused additional changes to the steady-state PL spectrum as shown in Figure 7b, notably a further hypsochromic shift and increase of the contribution of the G_4 component, along with a decrease of the spin-orbit splitting between G_1 and G_2 to 0.18 eV. Center positions are given in Table S4. Alendronate-modified NPs also had an increased apparent QY of 0.13, though the average PL lifetimes were not substantially different from the CA-NPs (Figure 7d). This result suggests that citric acid ligands act as static quenchers and that alendronate enhances passivation of the surface. Full TCSPC fits of CA-NPs and ALE-NPs are shown in Table 3.

Conjugation of Ce6 to ALE-NPs was accomplished through amide bond formation mediated by the coupling reagents NHS and DIC. Figure 8 shows absorbance measurements for ALE-NPs alone and ALE-NP-Ce6 conjugates, as well as a control reaction conducted without the coupling reagents NHS and DIC. The control sample retained a small amount of Ce6 after washing, suggesting that some may be free in solution or associated with the NPs non-covalently. In the conjugate sample, the Ce6 absorbance peaks located at 403 nm (Soret band), 525 & 641 nm (Q bands) are consistent with those reported previously for free Ce6 in PBS at pH <6[46]. The Ce6 concentrations were determined by comparing the absorbance values at the Q_x (0,0) peak (~640 nm) to a standard curve determined for free Ce6 in PBS pH ~3. The ε_{250} values of the conjugates were estimated to be ~10% greater than the ALE-NPs alone, an increase consistent with what would be expected by comparing the ε_{250} and ε_{400} values of Ce6 alone. The loading of Ce6 was ~0.44% w/w of the ALE-NPs, corresponding to ~1 Ce6 molecule/NP (calculations found in SI). The control sample contained roughly 1/10 the amount of Ce6, ~0.04% w/w.

The steady-state PL of NPs in the Ce6 conjugate sample was quenched with an efficiency $\eta = 0.52$ compared to an equal mass concentration of ALE-NPs alone, as shown in Figure 7e. A control reaction was conducted without Ce6 to confirm the PL quenching was not due to reactions with the DMSO or the

coupling reagents. The NP PL lifetimes were not significantly altered, in distinct contrast to the substantial steady-state quenching. They are shown in Figure 7f with fit details in Table 3.

The PL lifetimes of Ce6 in the conjugate samples provided additional evidence of energy transfer, through comparison of different excitation wavelengths: 400 nm light was used to excite Ce6 independently of the NPs, providing the "native" lifetimes in the absence of energy transfer from Ce^{3+}; 252 nm light was used to excite both Ce^{3+} and Ce6, with the lifetimes reflecting both direct excitation as well as energy transfer from Ce^{3+}. As shown in Figure 9 and Table 3, Ce6 PL lifetimes (measured at 660 nm, near the Ce6 emission peak) increased noticeably when the conjugates were excited at 252 nm versus 400 nm, from around 3.3 ns to 8.3 ns, suggesting that energy transfer from Ce^{3+} extends the excited state lifetime of the conjugated Ce6.

Discussion and conclusions

We have conducted a photophysical investigation of cerium and cerium-doped lanthanum fluoride nanoparticle-photosensitizer systems using newly described NP compositions designed to be of biologically relevant sizes and surface chemistries. A recent investigation of singlet oxygen production in theoretical nanoscintillator-photosensitizer systems suggested that careful optimization of excitation energies and NP-PS energy transfer efficiencies will be necessary to achieve a therapeutically relevant effect[21], though there have been relatively few experimental investigations of such systems. In particular, though cerium-doped LaF_3 is explicitly mentioned, it has not been hitherto established whether these NPs are effective as energy donors. They are potentially disadvantageous due to fluorescence lifetimes that are short compared to the long-lived phosphorescence of other luminescent lanthanides, but have favorable UV/blue emission that overlaps the strong Soret band shared by most porphyrin and chlorin-derived photosensitizers, and may additionally damage cells directly[47-49]. Our results suggest that both compositions of NPs studied are potentially efficient energy donors to PDT agents, though there are several considerations that should be taken into account to guide future work.

While energy transfer efficiency is typically estimated by the extent of quenching of steady-state and/or time-resolved donor luminescence in the presence of an acceptor, there are caveats for using these measures with our system. Because DPIX-DS, Ce6 and other PSs also absorb strongly at 252 nm, being excited directly and competitively with the Ce^{3+} absorption, changes in steady-state PL should not be assumed to be entirely due to increasing energy transfer when varying PS loading, especially in the case of $Ce_{0.1}La_{0.9}F_3/LaF_3$ NPs where DPIX-DS absorbs significantly more than the Ce^{3+}. It is perhaps more informative to consider the excitation spectrum of DPIX-DS when added to NPs, as shown in Figure 10 for CeF_3/LaF_3 NPs with 2% w/w DPIX-DS. Though direct excitation of DPIX-DS in the Soret band is certainly more

efficient, the Ce^{3+} excitation peaks appear distinctly, providing additional evidence of energy transfer. Time-resolved measurements provided further insight into energy transfer mechanisms, but are complicated by overlapping components that are quenched to different degrees. Energy transfer from NPs to DPIX-DS molecules was found to take place primarily in an indirect multi-step manner via the intermediate perturbed Ce^{3+} sites, which may have implications for NP preparation techniques (particularly regarding the crystallinity of the NPs) as well as energy transfer through scintillation.

The degree of PS loading with ALE-NP-Ce6 conjugates was much lower compared to the amounts investigated with DPIX-DS and ACA-NPs. The ~50% decrease in PL from NPs covalently bound to as few as 1 PS molecule on average, combined with little discernible effect on the time-resolved fluorescence curves (Figure 7d-f), is best explained by static quenching due to the formation of ground-state complexes. This implies energy transfer that occurs at a rate faster than 20 ps, consistent with the very short separation. Poisson statistics suggest that there are roughly equal populations of unconjugated NPs (with the same PL lifetimes exhibited by ALE-NPs) and conjugated NPs with excited state lifetimes shorter than the TCSPC instrument response.

The role of surface effects, such as those due to ligands and passivation through shelling, are important considerations for the purposes of optimizing NP-PS energy transfer. As shown in Figure S7, the Ce^{3+} emission components vary considerably between NP preparations. While a lack of passivation tends to dramatically reduce the luminescence yield of surface sites, their proximity to surface-bound PS and spectral overlaps are favorable. Addition of undoped LaF_3 shells can improve the luminescence yield at the expense of increased donor-acceptor separation and hypsochromic shift of the perturbed site band. An optimal shell thickness for energy transfer was indeed determined recently in a UCNP-PS system[50]. In that case, using Yb^{3+}-sensitized Er^{3+} upconversion, the quenching of donor luminescence lifetimes was found to be a better reflection of PS activation than steady-state emission quenching, diverging most in the region of highest efficiency. Though the efficiency of transfer with unshelled NPs was high, the singlet oxygen generation was far lower than with any of the shelled NPs due to their relatively low luminescence yield.

The approach to attaching/associating photosensitizer molecules with NPs also plays an important role in energy transfer and the effectiveness of the system. Electrostatic association of DPIX-DS with ACA-NPs, evidenced by a compromise in the colloidal stability of the complexes at PS amounts >6% w/w, has proven valuable for initial experiments, but is insufficient for preserving complexes under harsher conditions. Common approaches to preparing lanthanide-based NPs for use in physiological environments include polymer encapsulation and hydrophobic interactions, allowing for reasonable drug loading capacities of up to 8% w/w[16]. In these systems, drugs (photosensitizers or otherwise) are typically intercalated within the NP coating by virtue of their lipophilic nature. Though these methods allow for relatively easy loading,

covalent attachment may be preferable in order to maximize energy transfer, reduce bulk and control orientation and exposure of PS molecules. While alendronate provides an anchor for bioconjugation of PS molecules in close proximity to the NP surface, the colloidal stability of the NPs under physiological conditions remains problematic. Further modifications to the NP coating are under investigation, such as conjugation of mPEG molecules that may improve the stability and biocompatibility of the NPs.

Relative efficiencies will be sufficient to guide *in vitro* experiments. They can be evaluated through measurements of singlet oxygen production, the hallmark encompassing the overall effectiveness of the PS "activation." While singlet oxygen production is predicted to be the primary measure of biological efficacy in nanoscintillator-photosensitizer systems, unexpected synergies (or anti-synergies) also regularly arise when experiments are performed with living cells. For instance, cerium oxide NPs have been shown to have both radiosensitizing and radioprotective effects by virtue of the redox activity of cerium, with a significant dependence on pH and redox state of cerium, degree of surface exposure and energy of incident radiation[51-54]. Additionally, localization of photosensitizers within a cell, which determines the likely targets of generated singlet oxygen, is an important factor.

As the intention is to use the conjugates with ionizing radiation, it is ultimately the radioluminescence behavior of the NPs that is most pertinent. Wojtowicz *et al.* observed no substantial differences between the luminescence spectra of Ce-doped LaF_3 bulk crystals using optical excitation at 250 nm versus γ and β radiation from a Ru/Rh source, but this excitation independence has not been firmly established in NPs. Scintillation of cerium-doped LaF_3 NPs has only been demonstrated for nanocomposites where the NPs are embedded at high loading volumes into oleic acid or polymer hosts[55-57], materials that facilitate the scintillation of the NPs. Scintillation of colloidal NPs will be the subject of a future report from our groups.

Acknowledgements

Notes and references

ª Department of Biomedical Engineering and ᵇDepartment of Chemistry, McGill University, 3775 Rue University, Montreal, QC H3A 2B4, Canada.

E-mail: daniel.cooper@mail.mcgill.ca, jay.nadeau@mcgill.ca;

Fax: +1 514 398 7461; Tel: +1 514 398 8372

ᶜ Department of Chemistry, University of Southern California, Los Angeles, CA 90089, USA

ᵈ Department of Radiation Oncology, Keck School of Medicine, University of Southern California, Los Angeles, CA 90089, USA

1. D. Bechet, P. Couleaud, C. Frochot, M. L. Viriot, F. Guillemin and M. Barberi-Heyob, *Trends Biotechnol*, 2008, **26**, 612-621.
2. G. Charron, T. Stuchinskaya, D. R. Edwards, D. A. Russell and T. Nann, *The Journal of Physical Chemistry C*, 2012, **116**, 9334-9342.
3. D. K. Chatterjee, L. S. Fong and Y. Zhang, *Advanced Drug Delivery Reviews*, 2008, **60**, 1627-1637.
4. A. C. Samia, X. Chen and C. Burda, *Journal of the American Chemical Society*, 2003, **125**, 15736-15737.
5. B. C. Wilson and M. S. Patterson, *Physics in medicine and biology*, 2008, **53**, R61-109.
6. E. I. Zenkevich, E. I. Sagun, V. N. Knyukshto, A. S. Stasheuski, V. A. Galievsky, A. P. Stupak, T. Blaudeck and C. von Borczyskowski, *The Journal of Physical Chemistry C*, 2011, **115**, 21535-21545.
7. C. Fowley, N. Nomikou, A. P. McHale, P. A. McCarron, B. McCaughan and J. F. Callan, *Journal of Materials Chemistry*, 2012, **22**, 6456-6462.
8. C.-K. Lim, J. Heo, S. Shin, K. Jeong, Y. H. Seo, W.-D. Jang, C. R. Park, S. Y. Park, S. Kim and I. C. Kwon, *Cancer letters*, 2013, **334**, 176-187.
9. F. C. J. M. van Veggel, C. Dong, N. J. J. Johnson and J. Pichaandi, *Nanoscale*, 2012, **4**, 7309-7321.
10. M. Wang, G. Abbineni, A. Clevenger, C. Mao and S. Xu, *Nanomedicine : nanotechnology, biology, and medicine*, 2011, **7**, 710-729.
11. R. Naccache, E. M. Rodríguez, N. Bogdan, F. Sanz-Rodríguez, M. d. C. I. d. l. Cruz, Á. J. d. l. Fuente, F. Vetrone, D. Jaque, J. G. Solé and J. A. Capobianco, *Cancers*, 2012, **4**, 1067-1105.
12. D. K. Chatterjee, M. K. Gnanasammandhan and Y. Zhang, *Small*, 2010, **6**, 2781-2795.
13. X.-F. Qiao, J.-C. Zhou, J.-W. Xiao, Y.-F. Wang, L.-D. Sun and C.-H. Yan, *Nanoscale*, 2012, **4**, 4611-4623.
14. A. Zhou, Y. Wei, B. Wu, Q. Chen and D. Xing, *Molecular Pharmaceutics*, 2012, **9**, 1580-1589.
15. K. Liu, X. Liu, Q. Zeng, Y. Zhang, L. Tu, T. Liu, X. Kong, Y. Wang, F. Cao, S. A. G. Lambrechts, M. C. G. Aalders and H. Zhang, *ACS Nano*, 2012, **6**, 4054-4062.
16. C. Wang, H. Tao, L. Cheng and Z. Liu, *Biomaterials*, 2011, **32**, 6145-6154.
17. K. Kobayashi, N. Usami, E. Porcel, S. Lacombe and C. Le Sech, *Mutat Res*, 2010, **704**, 123-131.
18. J. D. Carter, N. N. Cheng, Y. Qu, G. D. Suarez and T. Guo, *The Journal of Physical Chemistry B*, 2007, **111**, 11622-11625.
19. S. J. McMahon, W. B. Hyland, M. F. Muir, J. A. Coulter, S. Jain, K. T. Butterworth, G. Schettino, G. R. Dickson, A. R. Hounsell, J. M. O'Sullivan, K. M. Prise, D. G. Hirst and F. J. Currell, *Sci. Rep.*, 2011, **1**.

20. P. Juzenas, W. Chen, Y.-P. Sun, M. A. N. Coelho, R. Generalov, N. Generalova and I. L. Christensen, *Advanced Drug Delivery Reviews*, 2008, **60**, 1600-1614.

21. N. Y. Morgan, G. Kramer-Marek, P. D. Smith, K. Camphausen and J. Capala, *Radiation Research*, 2009, **171**, 236-244.

22. Z. Luksiene, P. Juzenas and J. Moan, *Cancer letters*, 2006, **235**, 40-47.

23. Z. Luksiene, D. Labeikyte, B. Juodka and J. Moan, 2006, **25**, 293-306.

24. J. Takahashi and M. Misawa, *Radiation Physics and Chemistry*, 2009, **78**, 889-898.

25. L. Wang, W. Yang, P. Read, J. Larner and K. Sheng, *Nanotechnology*, 2010, **21**, 475103.

26. J. P. Scaffidi, M. K. Gregas, B. Lauly, Y. Zhang and T. Vo-Dinh, *ACS Nano*, 2011, **5**, 4679-4687.

27. A. Lempicki, A. J. Wojtowicz and E. Berman, *Nuclear Instruments and Methods in Physics Research Section A: Accelerators, Spectrometers, Detectors and Associated Equipment*, 1993, **333**, 304-311.

28. W. W. Moses and S. E. Derenzo, *Nuclear Science, IEEE Transactions on*, 1989, **36**, 173-176.

29. W. W. Moses and S. E. Derenzo, *Nuclear Instruments and Methods in Physics Research Section A: Accelerators, Spectrometers, Detectors and Associated Equipment*, 1990, **299**, 51-56.

30. W. W. Moses, S. E. Derenzo, M. J. Weber, A. K. Ray-Chaudhuri and F. Cerrina, *Journal of Luminescence*, 1994, **59**, 89-100.

31. A. J. Wojtowicz, M. Balcerzyk, E. Berman and A. Lempicki, *Physical Review B*, 1994, **49**, 14880-14895.

32. P. Dorenbos, *Physical Review B*, 2000, **62**, 15640-15649.

33. L. G. Jacobsohn, K. B. Sprinkle, S. A. Roberts, C. J. Kucera, T. L. James, E. G. Yukihara, T. A. DeVol and J. Ballato, *Journal of Nanomaterials*, 2011, **2011**.

34. L. G. Jacobsohn, A. Toncelli, K. B. Sprinkle, C. J. Kucera and J. Ballato, *Journal of Applied Physics*, 2012, **111**.

35. K. Kömpe, O. Lehmann and M. Haase, *Chemistry of Materials*, 2006, **18**, 4442-4446.

36. V. Sudarsan, F. C. J. M. van Veggel, R. A. Herring and M. Raudsepp, *Journal of Materials Chemistry*, 2005, **15**, 1332-1342.

37. C. Dong and F. C. J. M. van Veggel, *ACS Nano*, 2008, **3**, 123-130.

38. C. Dong, J. Pichaandi, T. Regier and F. C. J. M. van Veggel, *Nanoscale*, 2011, **3**, 3376-3384.

39. A. M. Cross, P. S. May, F. C. J. M. v. Veggel and M. T. Berry, *The Journal of Physical Chemistry C*, 2010, **114**, 14740-14747.

40. C. Dong, M. Raudsepp and F. C. J. M. van Veggel, *The Journal of Physical Chemistry C*, 2008, **113**, 472-478.

41. A. Brouwer, *Pure and Applied Chemistry*, 2011, **83**, 2213-2228.

42. J. Dairou, C. Vever-Bizet and D. Brault, *Photochemistry and Photobiology*, 2002, **75**, 229-236.

43. B. Valeur, *Molecular fluorescence : principles and applications*, Wiley-VCH, Weinheim; New York, 2002.

44. L. J. Tian, Y. J. Sun, Y. Yu, X. G. Kong and H. Zhang, *Chemical Physics Letters*, 2008, **452**, 188-192.

45. J. W. Stouwdam, G. A. Hebbink, J. Huskens and F. C. J. M. van Veggel, *Chemistry of Materials*, 2003, **15**, 4604-4616.

46. B. Čunderlíková, L. Gangeskar and J. Moan, *Journal of Photochemistry and Photobiology B: Biology*, 1999, **53**, 81-90.

47. W. Baumler, J. Regensburger, A. Knak, A. Felgentrager and T. Maisch, *Photochemical & photobiological sciences : Official journal of the European Photochemistry Association and the European Society for Photobiology*, 2012, **11**, 107-117.

48. A. Besaratinia, J. I. Yoon, C. Schroeder, S. E. Bradforth, M. Cockburn and G. P. Pfeifer, *FASEB journal : official publication of the Federation of American Societies for Experimental Biology*, 2011, **25**, 3079-3091.

49. J. Cadet, S. Mouret, J.-L. Ravanat and T. Douki, *Photochemistry and Photobiology*, 2012, **88**, 1048-1065.

50. Y. Wang, K. Liu, X. Liu, K. i. Dohnalová, T. Gregorkiewicz, X. Kong, M. C. G. Aalders, W. J. Buma and H. Zhang, *The Journal of Physical Chemistry Letters*, 2011, **2**, 2083-2088.

51. A. Briggs, S. Corde, S. Oktaria, R. Brown, A. Rosenfeld, M. Lerch, K. Konstantinov and M. Tehei, *Nanomedicine : nanotechnology, biology, and medicine*, 2013, **9**, 1098-1105.

52. G. Renu, V. V. D. Rani, S. V. Nair, K. R. V. Subramanian and V.-K. Lakshmanan, *Advanced Science Letters*, 2012, **6**, 17-25.

53. M. S. Wason, J. Colon, S. Das, S. Seal, J. Turkson, J. Zhao and C. H. Baker, *Nanomedicine : nanotechnology, biology, and medicine*, 2013, **9**, 558-569.

54. M. S. Wason and J. Zhao, *American journal of translational research*, 2013, **5**, 126-131.

55. P. Guss, R. Guise, D. Yuan, S. Mukhopadhyay, R. O'Brien, D. Lowe, Z. Kang, H. Menkara and V. V. Nagarkar, *Journal of Applied Physics*, 2013, **113**, 064303-064303-064306.

56. E. A. McKigney, R. E. Del Sesto, L. G. Jacobsohn, P. A. Santi, R. E. Muenchausen, K. C. Ott, T. Mark McCleskey, B. L. Bennett, J. F. Smith and D. Wayne Cooke, *Nuclear Instruments and Methods in Physics Research Section A: Accelerators, Spectrometers, Detectors and Associated Equipment*, 2007, **579**, 15-18.

57. E. A. McKigney, R. E. Muenchausen, D. W. Cooke, R. E. Del Sesto, R. D. Gilbertson, M. K. Bacrania, B. L. Bennett, L. G. Jacobsohn, T. M. McCleskey, K. C. Ott, S. C. Sitarz, J. F. Smith and S. Stange, 2007.
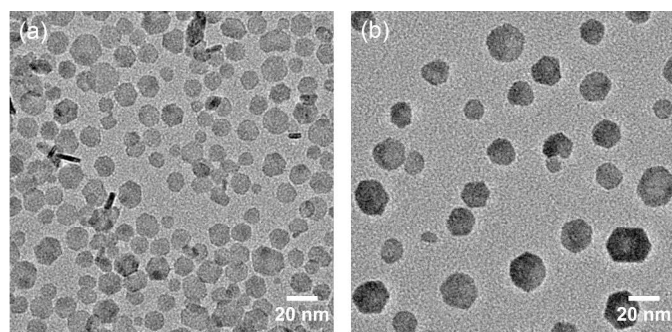
Fig. 1 TEM images of ACA-stabilized $Ce_{0.1}La_{0.9}F_3/LaF_3$ (a) and CeF_3/LaF_3 (b) NPs.
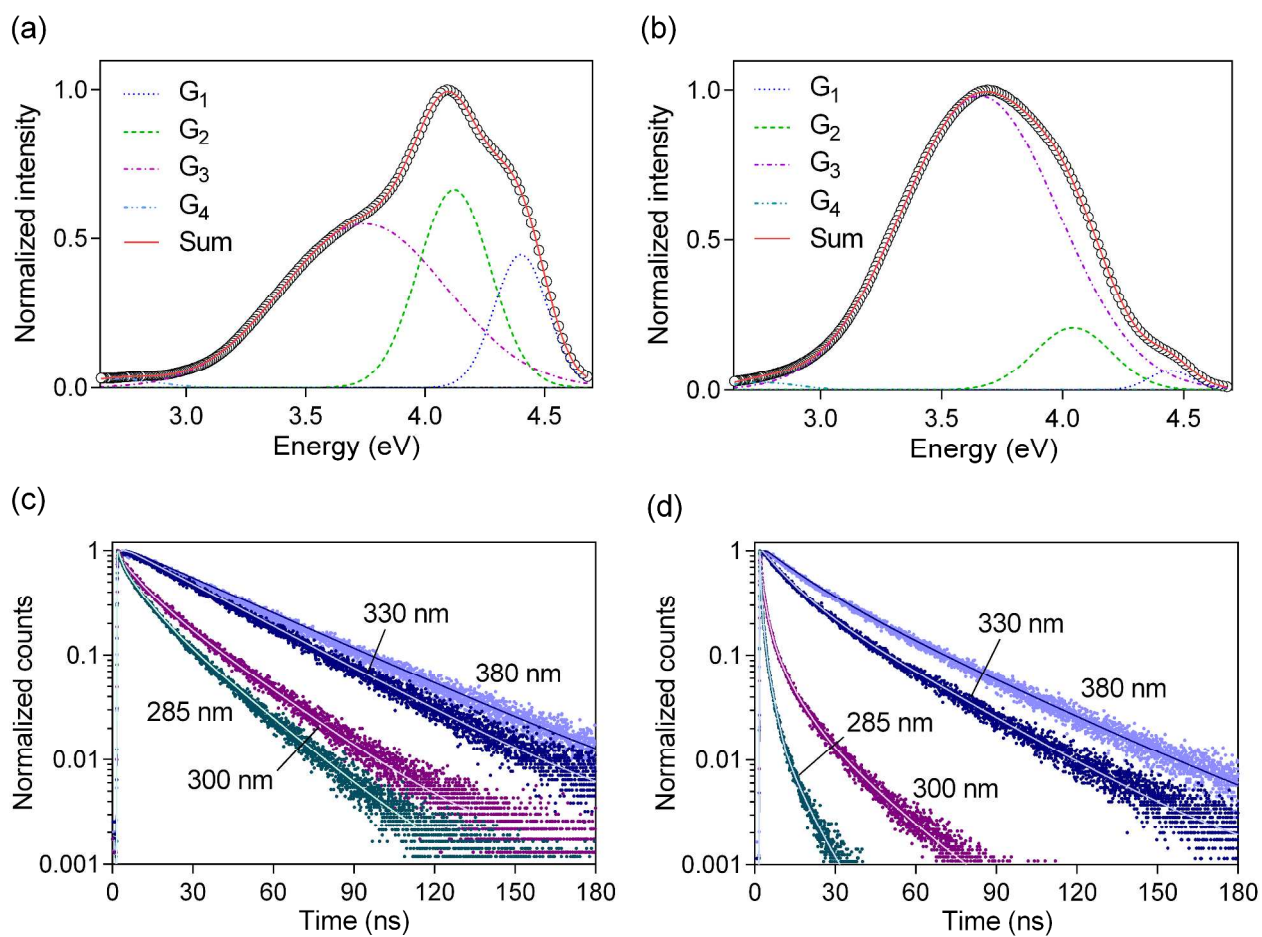
Fig. 2 (a,b) Steady-state emission spectra (black circles) and fits to Gaussian functions (sums shown as solid red lines) and (c,d) normalized PL lifetime decays and fits of ACA-stabilized (a,c) $Ce_{0.1}La_{0.9}F_3/LaF_3$ NPs at 50 µg/mL in water and (b,d) CeF_3/LaF_3 NPs at 10 µg/mL in water. With increased cerium concentration, there is a greater contribution of perturbed site emission, accompanied by a substantial reduction in the lifetimes of the emission measured at 285 nm (4.35 eV) and 300 nm (4.13 eV). Note similarities between 285 & 300 nm, and 330 (3.76 eV) & 380 nm (3.26 eV). The excitation wavelength was 252 nm (4.92 eV) for all data.

Table 1: Center positions of Gaussian fits of PL emission spectra shown in Figure 1a & b, and the relative contribution of the perturbed site band (G_3) to the total emission (A = area).

ACA-NP composition	μ_1 (eV)	μ_2 (eV)	μ_3 (eV)	μ_4 (eV)	A_3/A_{tot}	R^2
$Ce_{0.1}La_{0.9}F_3/LaF_3$	4.40	4.12	3.75	2.72	0.55	0.99
CeF_3/LaF_3	4.45	4.04	3.66	2.76	0.88	0.99
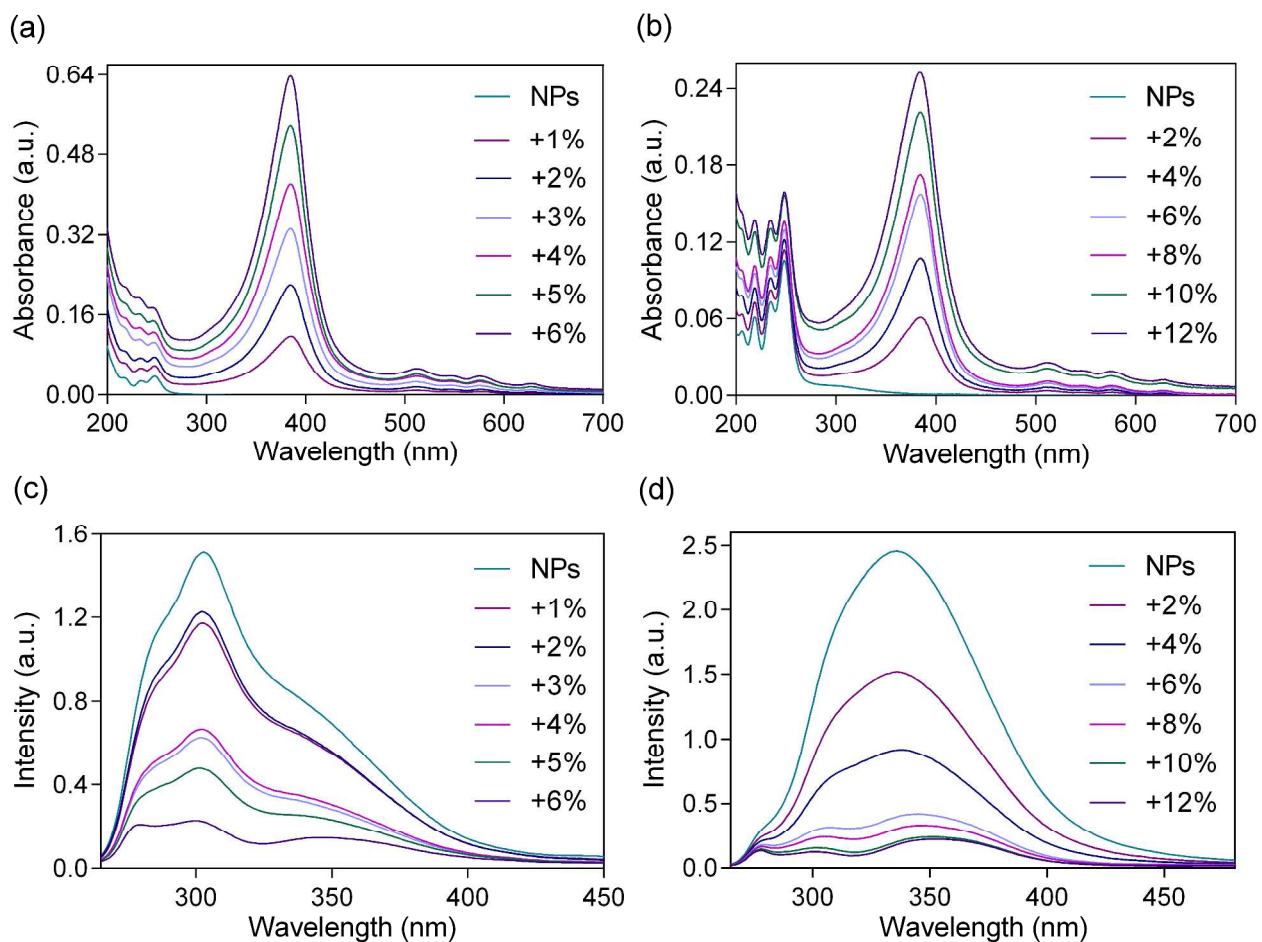
Fig. 3 Absorbance (a,b) and emission (c,d) spectra (excited at 252 nm) of ACA-stabilized (a,c) $Ce_{0.1}La_{0.9}F_3/LaF_3$ nanoparticles (500 µg/mL for absorbance and 50 µg/mL for emission) in water and (b,d) CeF_3/LaF_3 nanoparticles (100 µg/mL for absorbance and 10 µg/mL for emission) in water with increasing amounts of DPIX-DS, shown as % w/w.
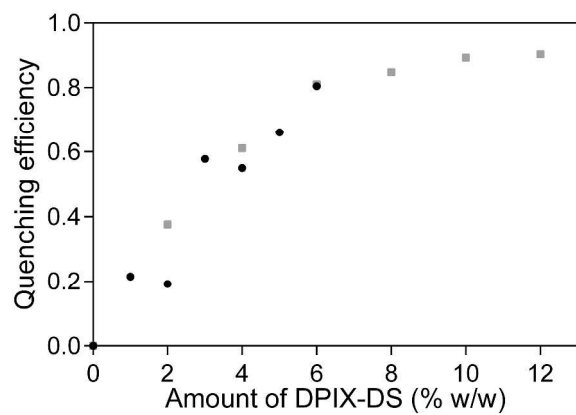
Fig. 4 Ce^{3+} PL quenching with increasing amounts of DPIX-DS for ACA-stabilized $Ce_{0.1}La_{0.9}F_3/LaF_3$ (circles) and CeF_3/LaF_3 (squares).

Journal Name

ARTICLE

Table 2 Average PL lifetimes for the ACA-NPs at different Ce^{3+} emission wavelengths. See Table S3 for additional details.

ACA-NP composition	τ_{ave} (ns) at 300 nm	τ_{ave} (ns) at 330 nm	τ_{ave} (ns) at 380 nm
$Ce_{0.1}La_{0.9}F_3/LaF_3$	20.3	32.5	38.8
CeF_3/LaF_3	8.3	24.0	31.8
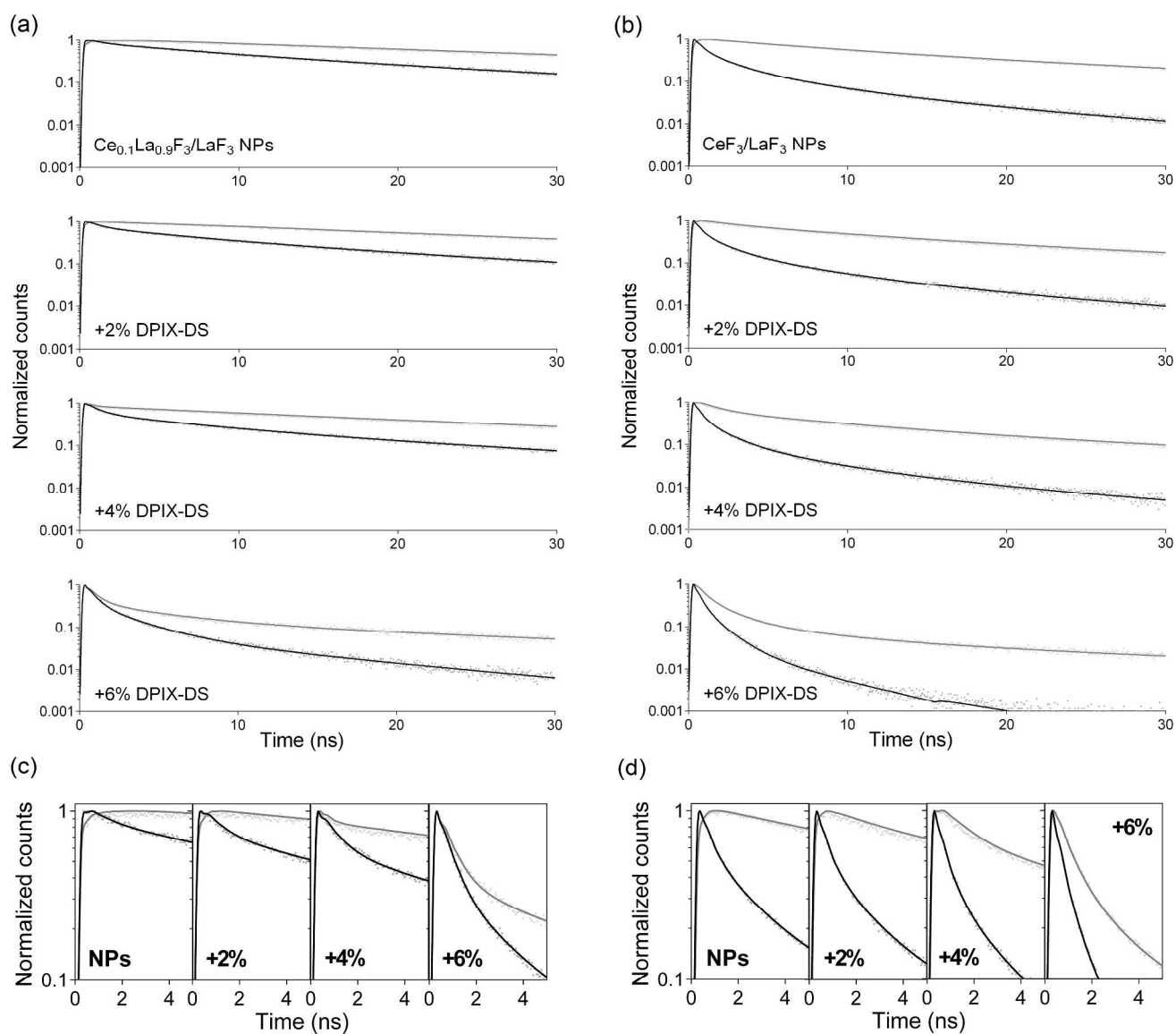
Fig. 5 Time-resolved Ce^{3+} PL quenching and fits at 300 (dark traces) & 330 nm (light traces) for ACA-stabilized (a, c) $Ce_{0.1}La_{0.9}F_3/LaF_3$ and (b, d) CeF_3/LaF_3 with 0, 2, 4 & 6% w/w DPIX-DS. Panels c & d show magnified sections of the traces in a & b, exhibiting the effect on 330 nm lifetimes at short times.
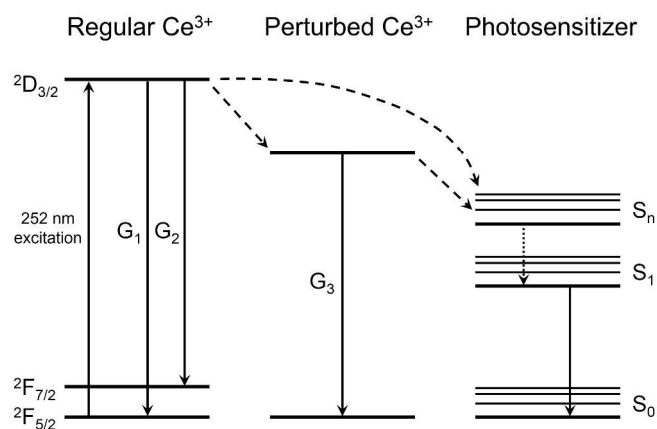
Scheme 1: Simplified Jablonski diagram illustrating the primary processes investigated in this work. Absorption/excitation and fluorescence are shown as solid lines, energy transfer routes shown as dashed lines, and internal conversion and vibrational relaxation of the PS combined as the dotted line. Non-radiative relaxation and quenching, as well as photosensitizer triplet states and intersystem crossing were omitted for simplicity.
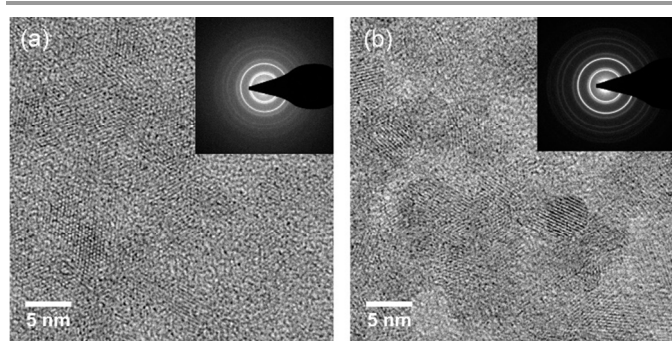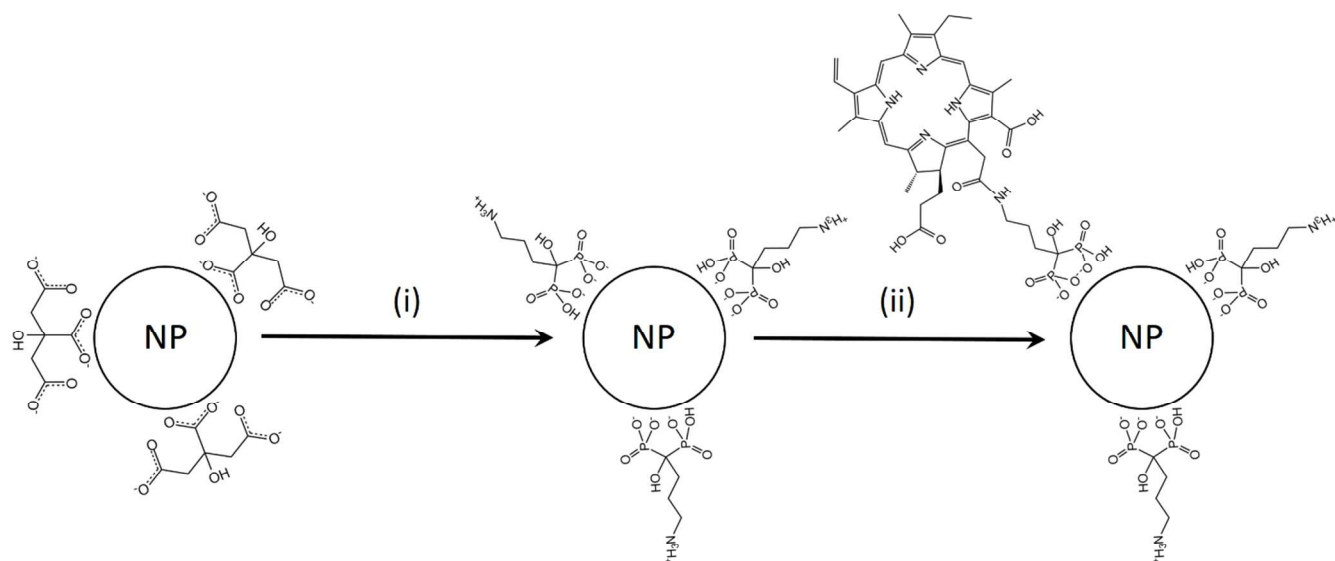
Fig. 6 TEM and SAED (insets) images of $Ce_{0.1}La_{0.9}F_3/LaF_3$ NPs (a) as-synthesized (coated with citrate) and (b) after ligand exchange with alendronate.

Journal Name

ARTICLE

Scheme 2 Preparation of NP-Ce6 conjugates. Reaction (i) represents ligand exchange, where the citrate ligands of the as-synthesized NPs are displaced by alendronate after stirring and heating for 2 hours in water. Reaction (ii) represents bioconjugation of chlorin e6, where chlorin e6 is covalently attached to the alendronate ligand through amide bond formation mediated by NHS & DIC, in a solution of primarily DMSO.
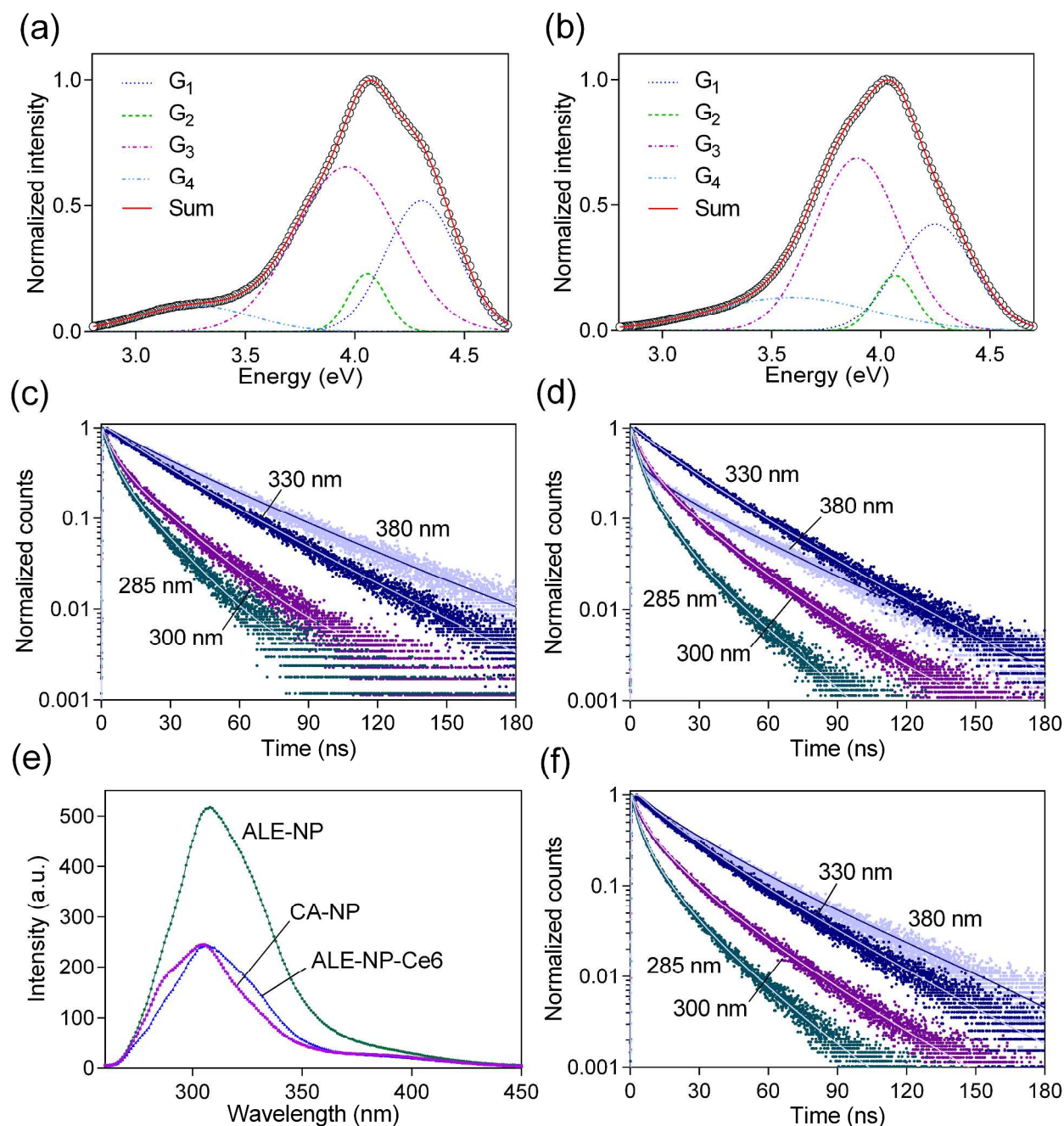
Fig. 7 (a,b) Steady-state emission spectra (black circles) and Gaussian fits (sum shown as solid red line) and (c,d) normalized PL lifetime decays and fits of (a,c) citrate-stabilized and (b,d) alendronate-stabilized $Ce_{0.1}La_{0.9}F_3/LaF_3$ NPs at 50 μg/mL in water. (e) Comparison of steady-state emission spectra of CA $Ce_{0.1}La_{0.9}F_3/LaF_3$ NPs, ALE-NPs and ALE-NP-Ce6 conjugates each at 50 μg/mL in water, using 252 nm excitation. Alendronate ligand exchange with alendronate altered the shape of the spectrum and increased the QY of the NPs approximately two-fold. Conjugation to Ce6 reduced the emission intensity by approximately half. (f) Normalized PL lifetime decays and fits of ALE-NP-Ce6 conjugates at 50 μg/mL in water. The average PL lifetimes did not change substantially compared to ALE-NPs (see Table 3 as well).

Table 3 Multiexponential fits of time-resolved PL measurements of citrate- and alendronate-stabilized $Ce_{0.1}La_{0.9}F_3/LaF_3$ NPs and Ce6 conjugates. Components with negative amplitudes were omitted. The "Conjugated Ce6 emission" measurements refer to emission at 660 nm from Ce6 that has been conjugated to ALE-NPs using excitation at either 252 nm or 400 nm, labeled accordingly. Confidence intervals for lifetimes greater than a few ns were typically less than ±5% of the fit value and less than ±1% for lifetimes greater than ~25 ns. For shorter lifetimes, confidence intervals were larger, up to ±50%.

CA $Ce_{0.1}La_{0.9}F_3/LaF_3$	I_1 (%)	τ_1 (ns)	I_2 (%)	τ_2 (ns)	I_3 (%)	τ_3 (ns)	I_4 (%)	τ_4 (ns)	$\langle\tau\rangle$ (ns)	χ^2
300 nm	—	—	1.2	0.32	22.5	5.2	76.3	20.7	16.9	1.0
330 nm	—	—	0.7	0.7	26.8	18	72.5	32.4	28.4	1.0
380 nm	—	—	—	—	38.2	24.4	61.8	45.6	37.6	0.99

ALE $Ce_{0.1}La_{0.9}F_3/LaF_3$	I_1 (%)	τ_1 (ns)	I_2 (%)	τ_2 (ns)	I_3 (%)	τ_3 (ns)	I_4 (%)	τ_4 (ns)	$\langle\tau\rangle$ (ns)	χ^2
300 nm	1	0.12	11.4	3	32.3	9.8	55.3	24.6	17.1	1.0
330 nm	—	—	—	—	19.5	13.3	80.5	28.9	26	1.0
380 nm	1.4	0.22	7.3	2.1	14.7	12.4	76.6	35.5	29.2	0.96

ALE-NP-Ce6 conjugate	I_1 (%)	τ_1 (ns)	I_2 (%)	τ_2 (ns)	I_3 (%)	τ_3 (ns)	I_4 (%)	τ_4 (ns)	$\langle\tau\rangle$ (ns)	χ^2
300 nm	1	0.13	13	3.4	36.2	11.4	49.8	25.8	17.4	1.0
330 nm	—	—	5.7	2.3	29	15.1	65.2	30.1	25.5	0.95
380 nm	—	—	5.2	4.7	62.5	24.1	32.3	54.2	33.6	1.0

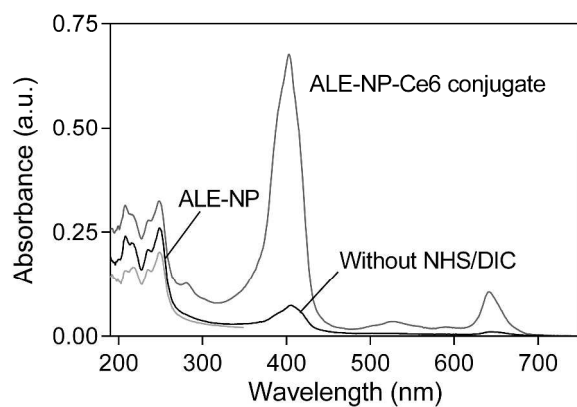| Conjugated Ce6 emission	I_1 (%)	τ_1 (ns)	I_2 (%)	τ_2 (ns)	I_3 (%)	τ_3 (ns)	I_4 (%)	τ_4 (ns)	$\langle\tau\rangle$ (ns)	χ^2
252 nm ex / 660 nm em	—	—	—	—	66.4	4.7	33.6	14.9	8.3	0.98
400 nm ex / 660 nm em	—	—	—	—	13	1.5	87	3.6	3.3	0.95

Fig. 8 Absorbance spectra of alendronate-stabilized $Ce_{0.1}La_{0.9}F_3/LaF_3$ NPs (ALE-NPs), ALE-NPs conjugated to Ce6 (ALE-NP-Ce6) and a control conjugation reaction without NHS & DIC. Note: samples were at different NP concentrations.
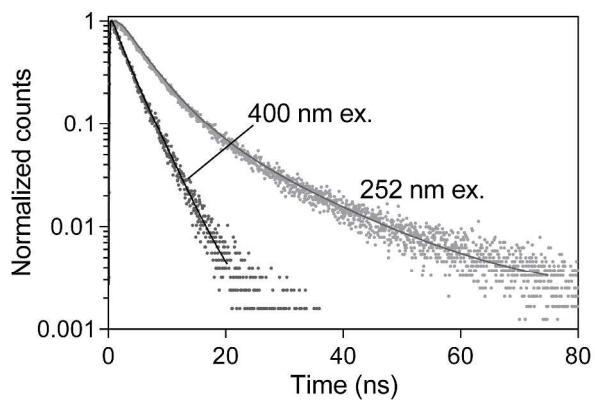
Fig. 9 Lifetime decays and fits of chlorin e6 emission (measured at 660 nm) when conjugated to alendronate-stabilized $Ce_{0.1}La_{0.9}F_3/LaF_3$ NPs. Excitation at 252 nm (direct excitation of Ce^{3+} and Ce6) resulted in longer lifetimes than direct excitation of Ce6 alone at 400 nm, suggestive of energy transfer from Ce^{3+} to Ce6 upon Ce^{3+} excitation.
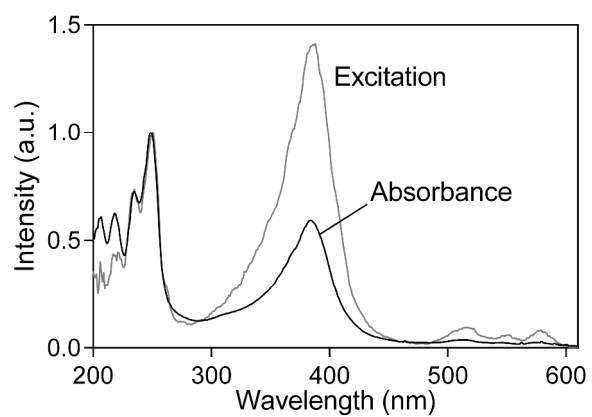
Fig. 10 Absorbance of ACA-stabilized CeF_3/LaF_3 NPs with 2% DPIX-DS and excitation spectrum of DPIX-DS (emission at 635 nm) of the same sample, normalized to the Ce^{3+} peaks at 250 nm. While direct excitation of DPIX-DS is more efficient, the distinct Ce^{3+} peaks in the excitation spectrum support NP-PS energy transfer.